

Supporting Information for

A Novel Hybrid Point Defect of Oxygen Vacancy and Phosphorus Doping in TiO₂ Anode for High-Performance Sodium Ion Capacitor

Daming Chen¹, Youchun Wu¹, Zhiqian Huang¹, Jian Chen^{1,*}

¹School of Materials Science and Engineering, Southeast University, Nanjing 211189, P. R. China

*Corresponding author. E-mail: j.chen@seu.edu.cn (J. C.)

Supplementary Figures and Tables

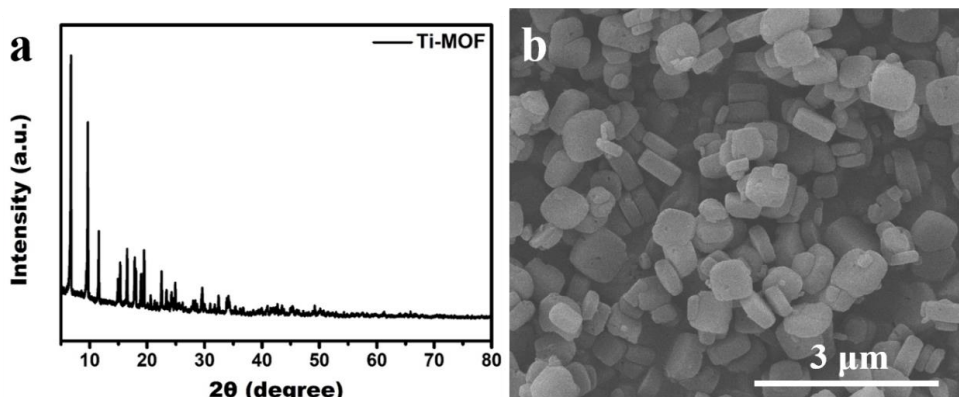


Fig. S1 a, b XRD pattern and SEM image of Ti-MOF

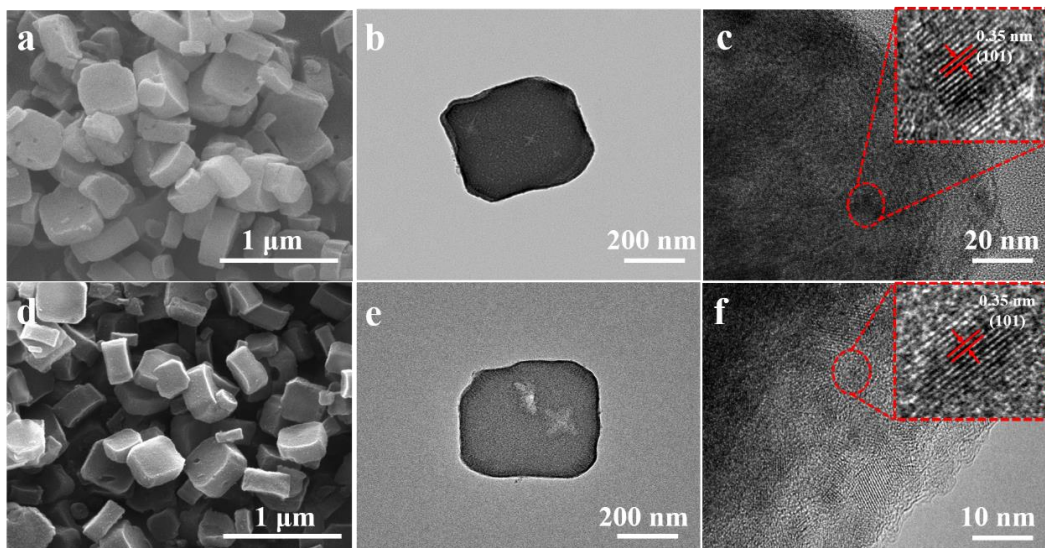


Fig. S2 a SEM image of TiO₂/C. **b** TEM image of TiO₂/C. **c** HRTEM image of TiO₂/C. **d** SEM image of TiO₂/C-P. **e** TEM image of TiO₂/C-P. **f** HRTEM image of TiO₂/C-P

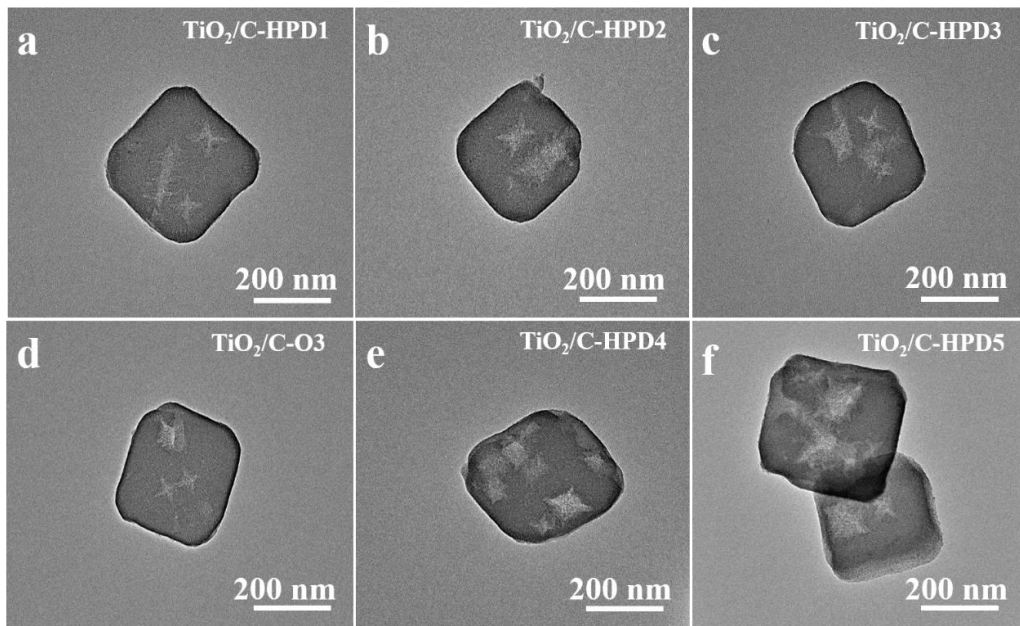


Fig. S3 a-f TEM images of TiO_2/C -HPD1, TiO_2/C -HPD2, TiO_2/C -HPD3, TiO_2/C -O3, TiO_2/C -HPD4 and TiO_2/C -HPD5, respectively

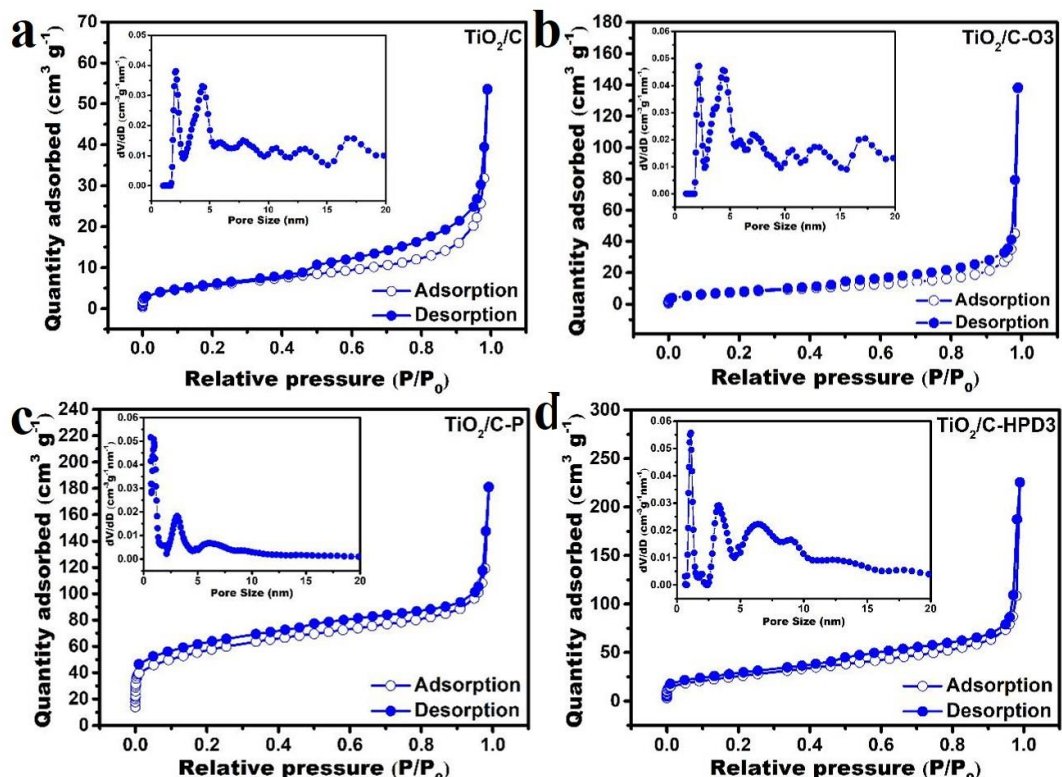


Fig. S4 N_2 adsorption-desorption isotherm and pore size distribution of the TiO_2/C , TiO_2/C -O3, TiO_2/C -P and TiO_2/C -HPD3, respectively

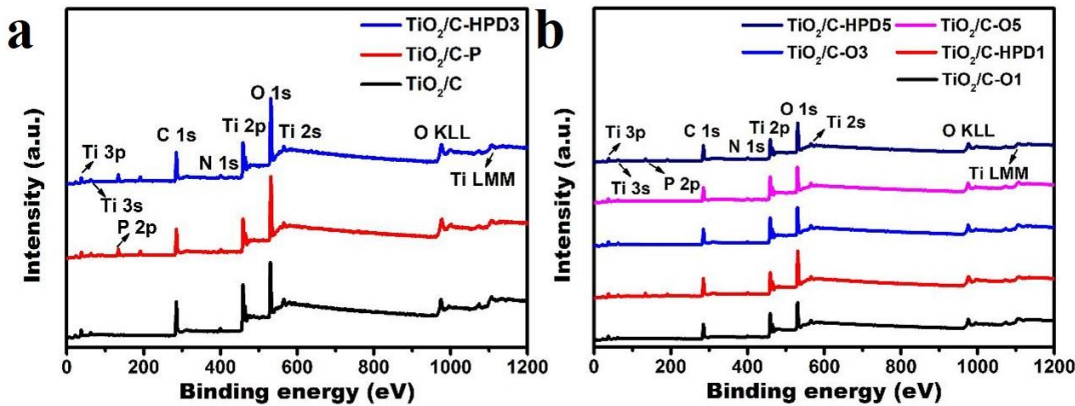


Fig. S5 a, b XPS spectra of the TiO_2/C , $\text{TiO}_2/\text{C-P}$, $\text{TiO}_2/\text{C-HPD}1$, $\text{TiO}_2/\text{C-O}1$, $\text{TiO}_2/\text{C-HPD}3$, $\text{TiO}_2/\text{C-O}3$, $\text{TiO}_2/\text{C-HPD}5$ and $\text{TiO}_2/\text{C-O}5$

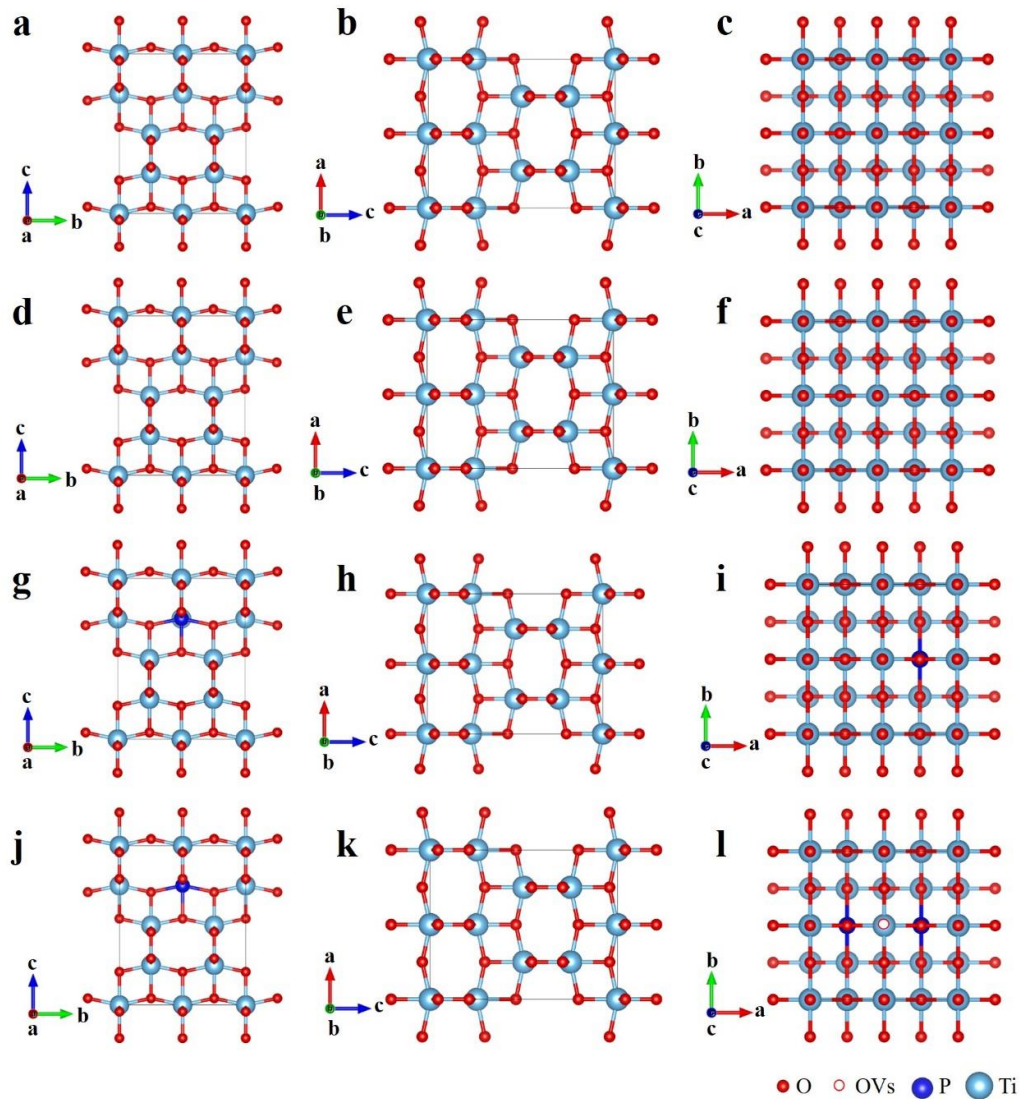


Fig. S6 a-c The structural models of TiO_2/C . **d-f** The structural models of $\text{TiO}_2/\text{C-O}3$. **g-i** The structural models of $\text{TiO}_2/\text{C-P}$ and **j-l** The structural models of $\text{TiO}_2/\text{C-HPD}3$

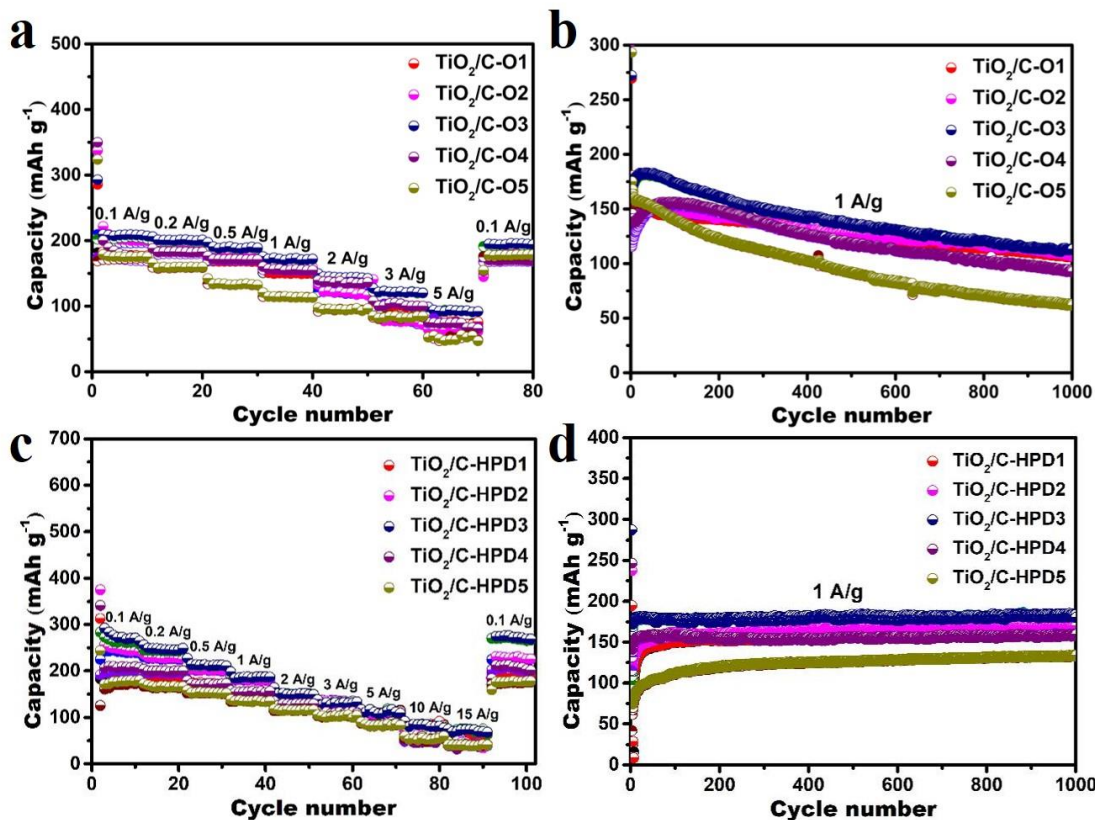


Fig. S7 **a, b** Rate performances and cycling performances of $\text{TiO}_2/\text{C-O1}$, $\text{TiO}_2/\text{C-O2}$, $\text{TiO}_2/\text{C-O3}$, $\text{TiO}_2/\text{C-O4}$ and $\text{TiO}_2/\text{C-O5}$. **c, d** Rate performances and cycling performances of $\text{TiO}_2/\text{C-HPD1}$, $\text{TiO}_2/\text{C-HPD2}$, $\text{TiO}_2/\text{C-HPD3}$, $\text{TiO}_2/\text{C-HPD4}$ and $\text{TiO}_2/\text{C-HPD5}$

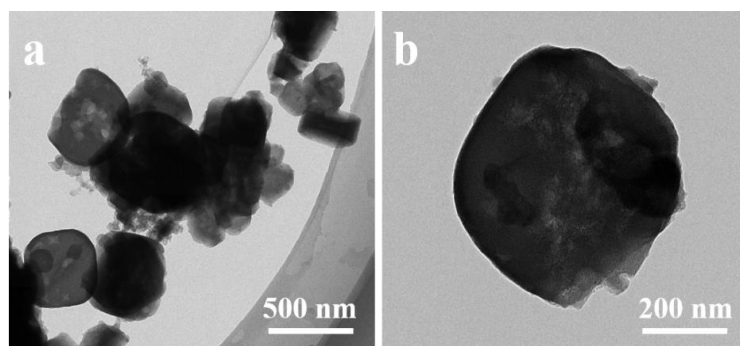


Fig. S8 **a, b** TEM images of $\text{TiO}_2/\text{C-HPD3}$ electrode after 500 cycles at 1 A g^{-1}

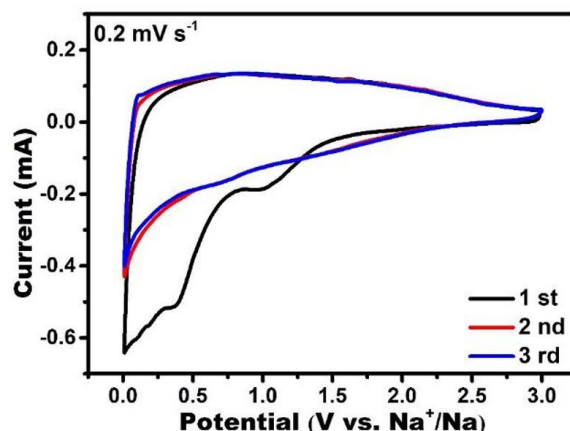


Fig. S9 Typical CV curves of the $\text{TiO}_2/\text{C-HPD3}$ at a scan rate of 0.2 mV s^{-1} within 0.01-3.0 V

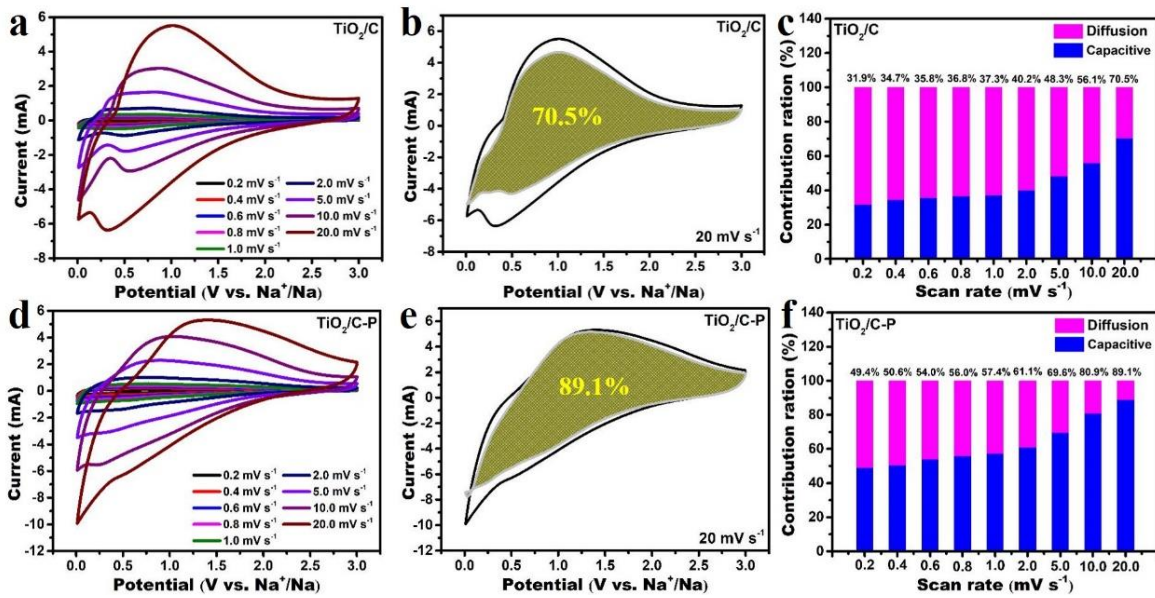


Fig. S10 **a** CV curves of TiO₂/C at various sweep rates. **b** CV curve with capacitive- and diffusion-controlled contributions at 20 mV s⁻¹. **c** Ratio of capacitive contribution in TiO₂/C at different scan. **d** CV curves of TiO₂/C-P at various sweep rates. **e** CV curve with capacitive- and diffusion-controlled contributions at 20 mV s⁻¹. **f** Ratio of capacitive contribution in TiO₂/C-P at different scan

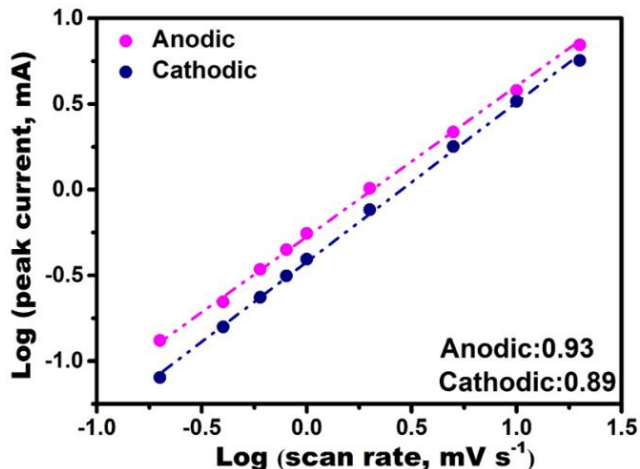


Fig. S11 Log (i) versus log (v) profile of TiO₂/C-HPD3

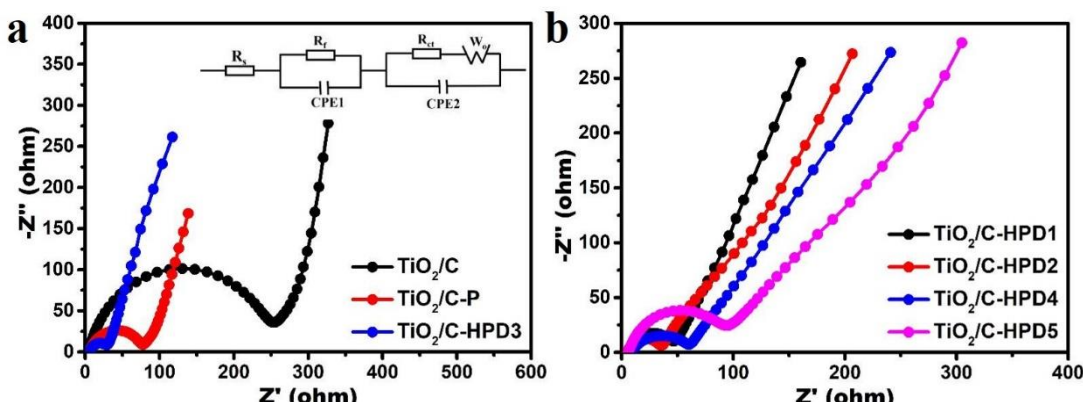


Fig. S12 **a**, **b** Nyquist plots of TiO₂/C, TiO₂/C-P, TiO₂/C-HPD1, TiO₂/C-HPD2, TiO₂/C-HPD3, TiO₂/C-HPD4 and TiO₂/C-HPD5; the insert section is the equivalent circuit

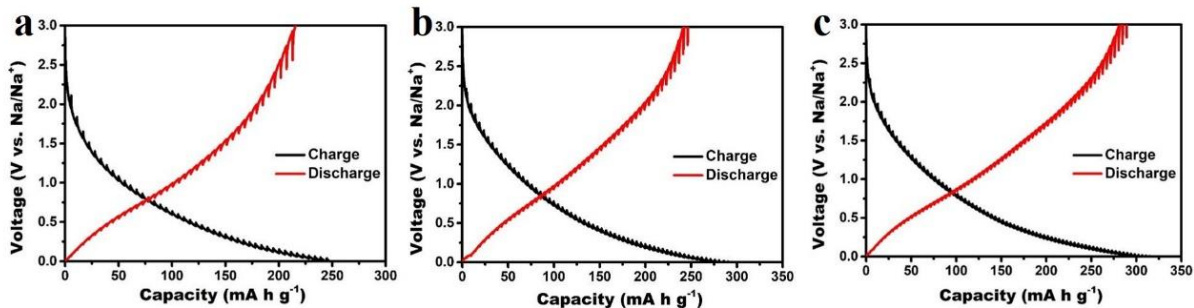


Fig. S13 GITT potential profiles of **a** TiO₂/C, **b** TiO₂/C-P and **c** TiO₂/C-HPD3

The diffusion coefficient (D_{Na^+}) in TiO₂/C, TiO₂/C-P and TiO₂/C-HPD3 electrodes can be calculated from the GITT potential profiles (with a 10 min constant current pulse of 50 mA followed by a relaxation process lasted 30 min) through Fick's second law according to the following equation:

$$D = \frac{4}{\pi\tau} \left(\frac{m_B V_M}{M_B S} \right)^2 \left(\frac{\Delta E_S}{\Delta E_\tau} \right)^2 \quad (\text{S1})$$

where τ represents the duration of the current pulse, m_B represents the mass of the active materials, V_M is the molar volume of the samples, M_B represents the molecular weight, S is the total surface electrode in contact with the electrolyte, ΔE_S denotes the quasi-thermodynamic equilibrium potential difference before and after the current pulse, ΔE_τ is the potential difference during current pulse.

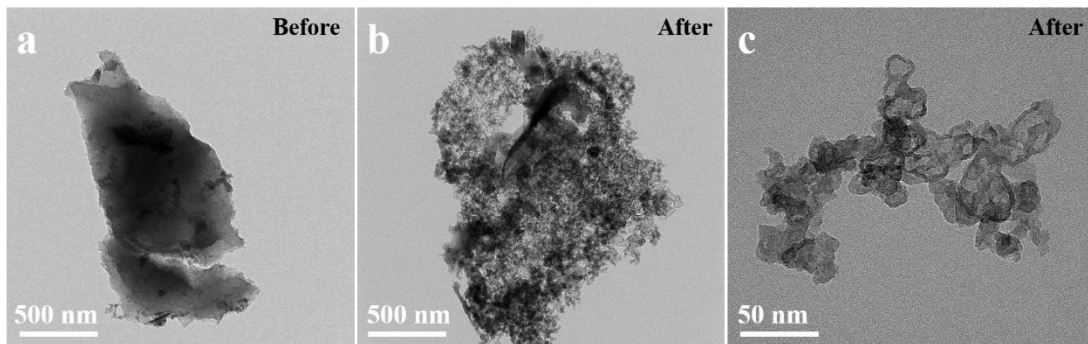


Fig. S14 **a-c** TEM images of the NPC before and after etching

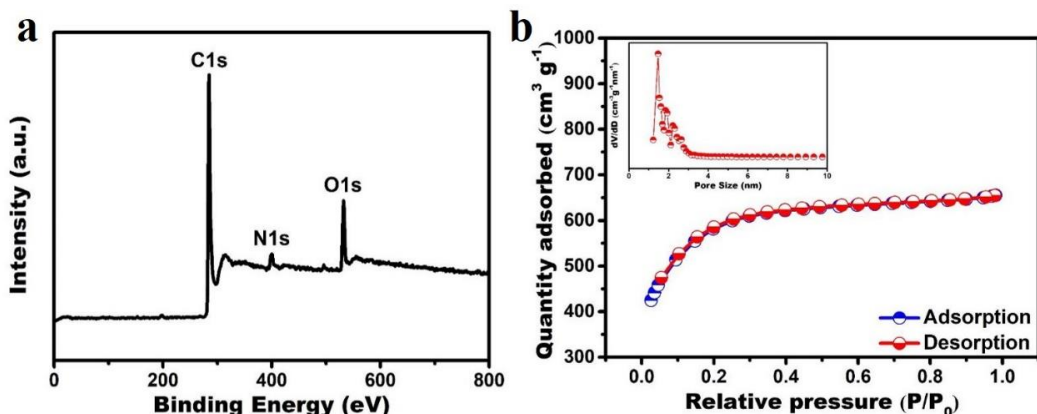


Fig. S15 **a** XPS spectra of the NPC. **b** N₂ adsorption-desorption isotherm and pore size distribution of the NPC

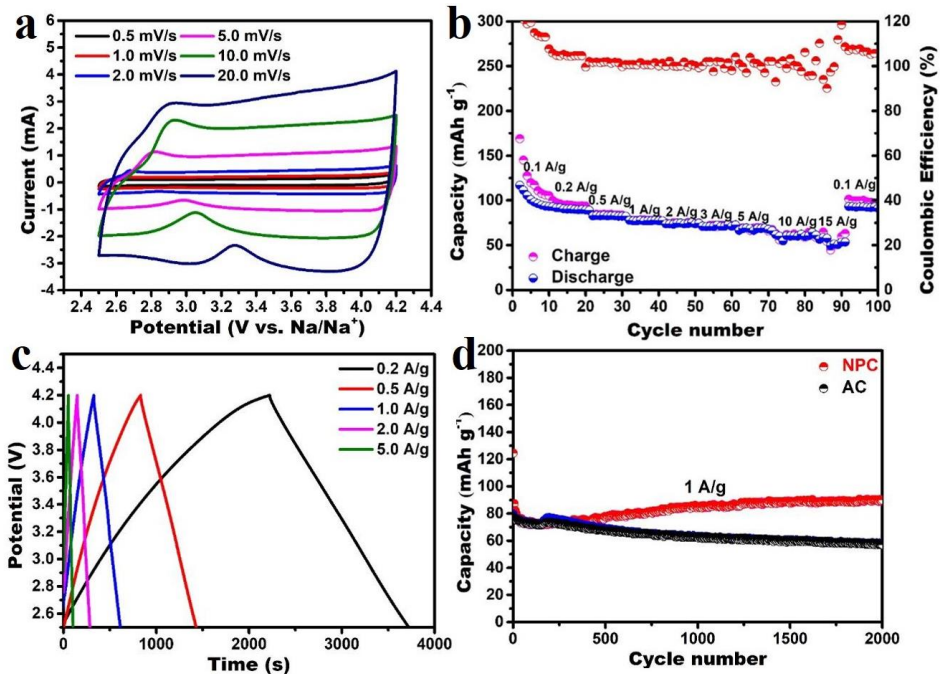


Fig. S16 Electrochemical performance of NPC: **a** CV curves at different scan rates, **b** rate performance, **c** GCD curves and **d** Cycling performances of NPC and AC at a current density of 1 A g^{-1}

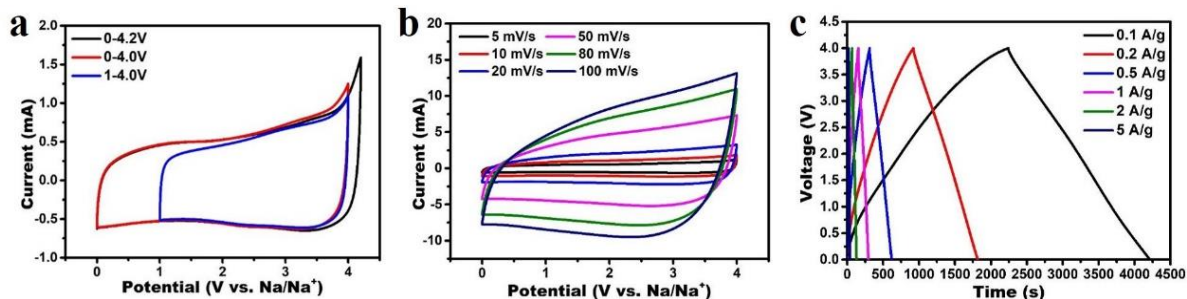


Fig. S17 **a** CV curves of $\text{TiO}_2/\text{C-HPD3}/\text{NPC}$ SICs at scan rate of 5 mV s^{-1} . **b** CV curves of at different scan rates. **c** Galvanostatic charge/discharge curves

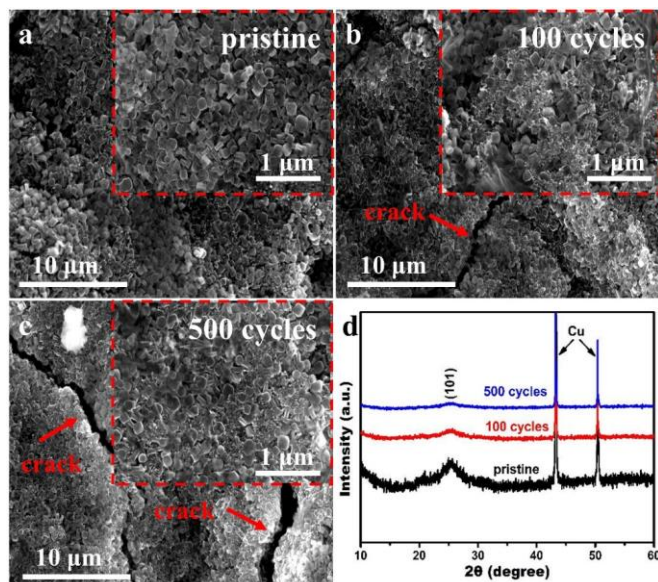


Fig. S18 **a-d** SEM images and XRD patterns of $\text{TiO}_2/\text{C-HPD3}$ electrodes after different cycles of $\text{TiO}_2/\text{C-HPD3}/\text{NPC}$ SICs at a current density of 2 A g^{-1}

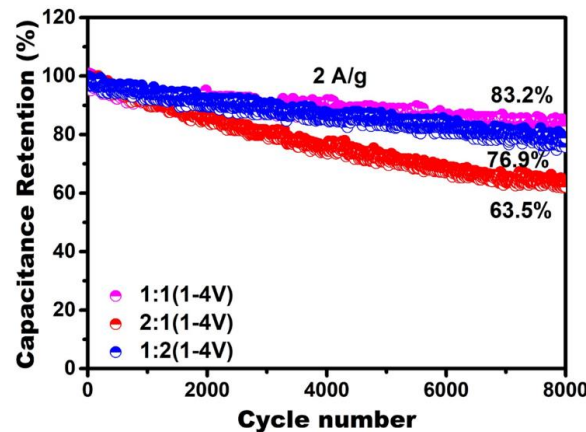


Fig. S19 Long-term cycle performance of TiO_2/C -HPD3//NPC SICs at different mass ratio

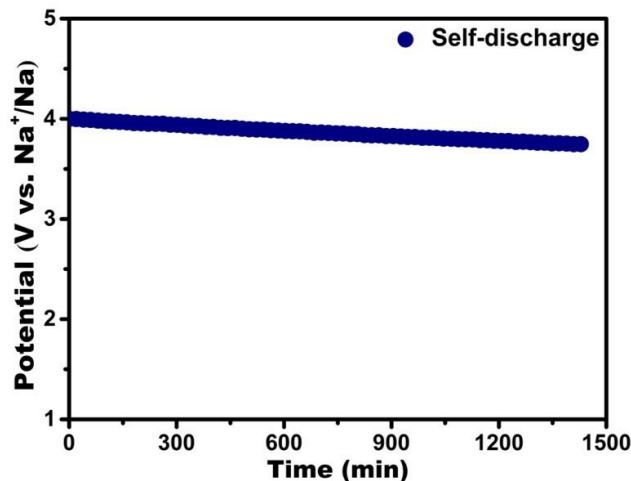


Fig. S20 Self-discharge curves of TiO_2/C -HPD3//NPC SICs after charging to 4V

Table S1 Ti^{3+} , OV_s, P, Ti-O-P and P-O-Ti content calculated from XPS results

Species	TiO_2/C	$\text{TiO}_2/\text{C-O1}$	$\text{TiO}_2/\text{C-O3}$	$\text{TiO}_2/\text{C-O5}$	$\text{TiO}_2/\text{C-P}$	$\text{TiO}_2/\text{C-HPD1}$	$\text{TiO}_2/\text{C-HPD3}$	$\text{TiO}_2/\text{C-HPD5}$
Ti^{3+}	9.05%	10.32%	10.88%	11.38%	-	-	-	-
OV _s	25.05 %	25.84%	26.94%	29.40%	-	-	-	-
P	-	-	-	-	6.75%	8.04%	9.17%	6.47%
Ti-O-P	-	-	-	-	13.91%	13.99%	16.39%	12.67%
P-O-Ti	-	-	-	-	22.76%	24.68%	33.81%	18.69%

Table S2 Adsorption energy of TiO_2/C , $\text{TiO}_2/\text{C-O3}$, $\text{TiO}_2/\text{C-P}$ and $\text{TiO}_2/\text{C-HPD3}$

Sample	Esodiated TiO_2/eV	ETiO ₂ /eV	E Na/eV	$\Delta E_{\text{Sodiation}}/\text{eV}$
TiO_2/C	-368.0925	-367.1483	-1.3353	0.3911
$\text{TiO}_2/\text{C-O3}$	-368.0925	-367.1483	-1.3353	0.2464
$\text{TiO}_2/\text{C-P}$	-356.6367	-355.1686	-1.3353	-0.1328
$\text{TiO}_2/\text{C-HPD3}$	-343.7680	-341.9331	-1.3353	-0.4996

Table S3 Comparison of sodium storage performance with reported Ti-based materials

Sample	Current density (A g ⁻¹)	Cycle number	Specific capacity (mAh g ⁻¹)	Rate capacity (current density)	Refs.
TiO₂/C-HPD3	0.2	300	239.4		
	1	1000	183.8	92.4 (10);	This work
	10	10000	84.1	82.5 (15)	
HTTFs-1h	0.2	200	188.7		[S1]
	5	10000	132.5	113.1 (10)	
TiO₂@TiOF₂-30h	0.5	2000	151.7		[S2]
	5	10000	101.2	115.4 (5)	
TiS₂/S-TiO₂/C	0.1	400	274		
	3	1500	161	114.2 (5)	[S3]
	10	10000	58		
TiO₂/C	0.1	300	206		[S4]
	10	10000	-	105 (10)	
TiO₂-S	0.1	200	236.3		[S5]
	1	1000	171.3	148.9 (2)	
TiO₂	0.1	100	207	110 (1)	[S6]
M-TiO₂@rGO	5	5000	123.3	142 (2)	[S7]
TiO₂(A/B)-MS	2.5	1000	-	50 (12.5)	[S8]
yolk@shell TiO_{2-x}	1	1000	99.8	68.6 (5)	[S9]
TiO₂/SCNT	3.35	1000	118	60 (16.75)	[S10]
S-TiO₂/CS	10	5000	100.5	120 (6.7)	[S11]
TiO₂-HS	5	4000	119	112 (12.8)	[S12]
N/S-TiO₂	0.5	1000	90	75 (1)	[S13]
P-TiO₂	3.35	1000	141	147 (3.35)	[S14]
TiO₂ nanosheets	0.5	2500	120	120 (1)	[S15]
TiO₂∩NPCSs	0.67	3000	152	85 (13.4)	[S16]
TiO₂	0.5	1400	98	102 (1.5)	[S17]
TiO₂@Ti₃C₂T_x	0.96	5000	110	68 (3.84)	[S18]

Table S4 Impedance parameters of the fitting equivalent circuit

Sample	R _s (Ω)	R _f (Ω)	R _{ct} (Ω)
TiO₂/C	7.43	265.8	594.8
TiO₂/C-P	2.86	152.9	417.0
TiO₂/C-HPD1	2.35	141.7	315.8
TiO₂/C-HPD2	1.83	128.4	308.4
TiO₂/C-HPD3	1.55	112.6	226.5
TiO₂/C-HPD4	1.98	135.6	296.0
TiO₂/C-HPD5	3.87	181.4	375.1

Supplementary References

- [S1] P. Xue, Q. Li, W. Gong, Z. Sun, H. Wang et al., Structure-induced partial phase transformation endows hollow TiO₂/TiN heterostructure fibers stacked with nanosheet arrays with extraordinary sodium storage performance. *J. Mater. Chem. A* **9**(20), 12109-12118 (2021). <https://doi.org/10.1039/d1ta01729b>
- [S2] S. Guan, Q. Fan, Z. Shen, Y. Zhao, Y. Sun et al., Heterojunction TiO₂@TiOF₂ nanosheets as superior anode materials for sodium-ion batteries. *J. Mater. Chem. A* **9**(9), 5720-5729 (2021). <https://doi.org/10.1039/d0ta12340d>
- [S3] Y. Zhang, Y. Huang, V. Srot, P.A. Aken, J. Maier et al., Enhanced pseudo-capacitive contributions to high-performance sodium storage in TiO₂/C nanofibers via double effects of sulfur modification. *Nano-Micro Lett.* **12**, 165 (2020). <https://doi.org/10.1007/s40820-020-00506-1>
- [S4] H. Li, J. Lang, S. Lei, J. Chen, K. Wang et al., A high-performance sodium-ion hybrid capacitor constructed by metal-organic framework-derived anode and cathode materials. *Adv. Funct. Mater.* **28**(30), 1800757 (2018). <https://doi.org/10.1002/adfm.201800757>
- [S5] M. Kang, Y. Wu, X. Huang, K. Zhou, Z. Huang et al., Engineering of a TiO₂ anode toward a record high initial coulombic efficiency enabling high-performance low-temperature Na-ion hybrid capacitors. *J. Mater. Chem. A* **6**(45), 22840-22850 (2018). <https://doi.org/10.1039/c8ta07127f>
- [S6] W. Feng, R.R. Maça, V. Etacheri, High-energy-density sodium-ion hybrid capacitors enabled by interface-engineered hierarchical TiO₂ nanosheet anodes. *ACS Appl. Mater. Interfaces* **12**(4), 4443-4453 (2020). <https://doi.org/10.1021/acsmi.9b17775>
- [S7] Y. Fang, Y. Zhang, C. Miao, K. Zhu, Y. Chen et al., Mxene-derived defect-rich TiO₂@rGO as high-rate anodes for full na ion batteries and capacitors. *Nano-Micro Lett.* **12**, 128 (2020). <https://doi.org/10.1007/s40820-020-00471-9>
- [S8] J.Y. Hwang, H.L. Du, B.N. Yun, M.G. Jeong, J.S. Kim et al., Carbon-free TiO₂ microspheres as anode materials for sodium ion batteries. *ACS Energy Lett.* **4**(2), 494-501 (2019). <https://doi.org/10.1021/acsenergylett.8b02510>
- [S9] Z. Chen, L. Xu, Q. Chen, P. Hu, Z. Liu et al., Spray-pyrolysis-assisted synthesis of yolk@shell anatase with rich oxygen vacancies for efficient sodium storage. *J. Mater. Chem. A* **7**(12), 6740-6746 (2019). <https://doi.org/10.1039/c8ta11440d>
- [S10] S. Luo, T. Yuan, L. Soule, J. Ruan, Y. Zhao et al., Enhanced ionic/electronic transport in nano-TiO₂/sheared cnt composite electrode for Na⁺ insertion-based hybrid ion-capacitors. *Adv. Funct. Mater.* **30**(5), 1908309 (2020). <https://doi.org/10.1002/adfm.201908309>
- [S11] Y. Zhang, X. He, J. Tang, J. Jiang, X. Ji et al., Sulfur-doped TiO₂ anchored on a large-area carbon sheet as a high-performance anode for sodium-ion battery. *ACS Appl. Mater. Interfaces* **11**(47), 44170-44178 (2019). <https://doi.org/10.1021/acsmi.9b14597>
- [S12] X. Xu, B. Chen, J. Hu, B. Sun, X. Liang et al., Heterostructured TiO₂ spheres with tunable interiors and shells toward improved packing density and pseudocapacitive sodium storage. *Adv. Mater.* **31**(46), e1904589 (2019). <https://doi.org/10.1002/adma.201904589>
- [S13] W. Song, H. Zhao, L. Wang, S. Liu, Z. Li, Co-doping nitrogen/sulfur through a solid-

state reaction to enhance the electrochemical performance of anatase TiO₂ nanoparticles as a sodium-ion battery anode. *ChemElectroChem* **5**(2), 316-321 (2018). <https://doi.org/10.1002/celc.201701015>

- [S14] J. Ni, S. Fu, Y. Yuan, L. Ma, Y. Jiang et al., Boosting sodium storage in TiO₂ nanotube arrays through surface phosphorylation. *Adv. Mater.* **30**(6), 1704337 (2018). <https://doi.org/10.1002/adma.201704337>
- [S15] R.R. Maça, D.C. Juárez, M.C. Rodríguez, V. Etacheri, Nanointerface-driven pseudocapacitance tuning of TiO₂ nanosheet anodes for high-rate, ultralong-life and enhanced capacity sodium-ion batteries. *Chem. Eng. J.* **391**, 123598 (2020). <https://doi.org/10.1016/j.cej.2019.123598>
- [S16] J. Feng, Y. Dong, Y. Yan, W. Zhao, T. Yang et al., Extended lattice space of TiO₂ hollow nanocubes for improved sodium storage. *Chem. Eng. J.* **373**, 565-571 (2019). <https://doi.org/10.1016/j.cej.2019.05.065>
- [S17] X. Wang, L. Qi, H. Wang, Anatase TiO₂ as a Na⁺-storage anode active material for dual-ion batteries. *ACS Appl. Mater. Interfaces* **11**(33), 30453-30459 (2019). <https://doi.org/10.1021/acsami.9b09703>
- [S18] X. Guo, J. Zhang, J. Song, W. Wu, H. Liu et al., MXene encapsulated titanium oxide nanospheres for ultra-stable and fast sodium storage. *Energy Storage Mater.* **14**, 306-313 (2018). <https://doi.org/10.1016/j.ensm.2018.05.010>